Incorporating Directionality in Transversal-Resonator-Based Bandpass Filters With Tunable Transfer Function Characteristics

Zixiao Zhang, *Graduate Student Member, IEEE*, and Dimitra Psychogiou, *Senior Member, IEEE*

***Abstract*— This paper introduces a detailed methodology for the realization of multi-functional transversal resonator-based non-reciprocal bandpass filters (NR-BPFs) that combine the functionality of a single-/multi-band BPF and an RF isolator. Directionality is achieved through spatiotemporal modulation (STM) whereas transfer function reconfigurability is obtained by only tuning the resonant frequency of its constituent resonators. A detailed design methodology to synthesize the response of transversal resonator-based STM arrays is introduced in this work for the first time, facilitating the synthesis of advanced RF filtering transfer functions based of transversal resonator arrays with incorporated directionality. The operating principles and scalability of the design method are demonstrated through the analysis of four distinct transversal resonator-based STM filtering topologies that facilitate the realization of high-order and highly-modular single-band and multi-band transfer functions with multiple levels of RF tuning including frequency tuning, bandwidth tuning, band controllability, and intrinsic switch-off capabilities. The concept has been validated at UHF band through the manufacturing and testing of four lumped-element NR-BPFs.**

***Index Terms*— Bandpass filter (BPF), non-reciprocity, spatial-temporal modulation (STM).**

I. Introduction

EMERGING wireless communication systems are increasingly in need of highly-reconfigurable multi-functional RF components to enhance the link performance and enable challenging applications such as full-duplex spectrum usage or joined sensing and communications (JCAS). In this regard, non-reciprocal devices such as RF isolators and circulators are essential for isolating different parts of their RF front-ends (e.g., separating transmit from receive paths) and cancelling inter-stage reflections, with the aim of improving the signal-to-noise (SNR) ratio [1], [2]. Furthermore, reconfigurability alongside RF filtering is also needed in the RF front-ends to ensure adaptability to dynamically changing spectral conditions and to provide robust interference suppression.

Manuscript received 29 May 2023; revised 21 July 2023 and 22 August 2023; accepted 17 September 2023. Date of publication 20 October 2023; date of current version 18 December 2023. This work was supported by the Science Foundation Ireland (SFI) under Project 20/RP/8334. This article was recommended by Associate Editor M. A. Abdulaziz. *(Corresponding author: Zixiao Zhang.)*

The authors are with the School of Engineering, University College Cork, Cork, T12 K8AF Ireland, and also with the Tyndall National Institute, Cork, T12 R5CP Ireland (e-mail: zixiao.zhang@tyndall.ie; DPsychogiou@ucc.ie).

Color versions of one or more figures in this article are available at https://doi.org/10.1109/TCSI.2023.3320036.

Digital Object Identifier 10.1109/TCSI.2023.3320036

Spatiotemporal modulation (STM) has recently been investigated as an alternative circuit design approach for incorporating directionality within RF components as opposed to traditional bulky ferrite-based approaches [3], [4], [5], [6] or power-hungry transistor-based elements [7], [8], [9], [10]. Examples of this trend include directional transmission lines [11], [12], RF filters [13], [14], [15], [16], [17], [18], [19], [20], [21], [22], [23], [24], power dividers [25] and antennas [26], [27], [28], [29]. Directionality is accomplished by breaking the time reversal symmetry either by modulating arrays of capacitors or the resonant frequency of resonators. STM has also been exploited for the realization of non-reciprocal bandpass filters (NR-BPFs) due to the advantage of integrating the functions of a BPF and an RF isolator into a single, co-designed RF component, thereby reducing the overall size of the RF front ends. An STM NR-BPF was first demonstrated in [13] by modulating its constituent in-line resonators through successively phase-shifted low frequency AC signals. Using as a basis this approach, alternative integration schemes for STM-based BPFs have been presented using acoustic-wave resonators [14], [15], lumped-element configurations [16], [17], [18], and microstrip-based RF filtering components [19], [20], [21], [22], [23], [24]. However, the majority of the reported NR-BPFs either work at low frequencies (e.g. up to 250 MHz in [17]), or have static transfer functions [13], [19], [20], [23], or have high insertion loss (IL: 6.5 dB) [15] or low isolation (IL< 12 dB) [23] or their transfer function can only be tuned in terms of center frequency [21], [22], [24], rendering them unable to meet the high levels of agility required in emerging communication systems. Only a couple of tunable NR-BPF topologies featuring multiple levels of RF tuning [16] or multi-band transfer functions [17], [18] have been demonstrated to date. They are mostly based on inline resonator configurations in which tuning elements are incorporated in both their resonators and their impedance inverters for a fully tunable transfer function to be realized. This requirement makes their realization complex, lossy, and challenging to optimize.

This paper presents a comprehensive design methodology and a practical validation concept for transversal-resonator-based NR-BPF with widely-tunable transfer function characteristics, high levels of isolation between the forward and the backward direction and multiple levels of single and multi-band transfer function tuning. Specifically, the manuscript demonstrates for the first time how to model transversal STM resonator-based arrays that in turn facilitate the synthesis of advanced RF filtering transfer functions with incorporated directionality.

The operating principles of the transversal-resonator-based NR-BPF concept and its scalability to highly-selective transfer functions are discussed through its application to four distinct high order filtering topologies. They include a single-band BPF based on two cascaded transversal cells (Topology 1), a single-band fourth-order box-like NR-BPF (Topology 2), a single-band sixth-order box-like NR-BPF (Topology 3), and a six-resonator-based NR-BPF using three series transversal cells (Topology 4), which exhibits multiple levels of transfer function tunability alongside a dual-band response. Multi-levels of RF tuning can be obtained for the four topologies using a simple RF tuning mechanism where only the resonant frequencies of the resonators are altered. These include center frequency tuning, bandwidth (BW) tuning and intrinsic switching off for all the four topologies, as well as flexible band controllability for Topology 4. For all of the aforementioned tuning states, high levels of IS ($>$ 20 dB) between the forward and the reverse direction can be obtained. When compared to a conventional solution where an amplifier is cascaded in series with a tunable BPF to incorporate non-reciprocity alongside amplification, the STM-based NR-BPFs of this work have significantly smaller size. They don't consume any power, nor generate any heating nor require inter-stage matching networks or harmonic terminations. Furthermore, they allow for dynamic reconfiguration of the direction of propagation.

The manuscript is organized as follows. Section II establishes the theoretical foundations for the transversal resonator-based concept and demonstrates how STM doublets can be modelled using a simple synthesis method. Whereas spectral network parameter matrices of a time-varying resonator have been developed in [30], and applied in in-line BPF configurations [13], this method has not yet been applied to STM transversal cells, which serve as the foundational counterpart for a wide variety of filters. In Section III, a comprehensive design procedure is discussed for selecting the STM parameters for these filters with the purpose of achieving high directivity. The experimental validation of the concept for all four filtering topologies is discussed in Section IV. Finally, Section V highlights the main contributions of this work.

II. Analysis of Spatiotemporally-Modulated Transversal Resonator-Based BPFs

The details of the STM two-resonator transversal cell or doublet are illustrated in Fig. 1 in terms of its coupling routing diagram (CRD) [Fig. 1(a)] and its circuit equivalent [Fig. 1(b)]. The doublet, denoted by its ABCD matrix $\mathbf{N_t}$, can be considered as the parallel connection of two networks marked in blue and red, with their respective ABCD matrices being $\mathbf{N_1}$ and $\mathbf{N_{11}}$. The red (blue) network comprises a cascaded connection of an input inverter $M_{1,2}$ ($M_{1,3}$), an STM resonator R_1 (R_2) and an output inverter $M_{2,4}$ ($M_{3,4}$). The circuit equivalent of the STM doublet is provided in Fig.1 (b), where the STM resonators are implemented as parallel LC tanks whose capacitors are time-variant with capacitance $C_{0x}(t)$ as given in (1) and their inductors L_x (x is the index number of

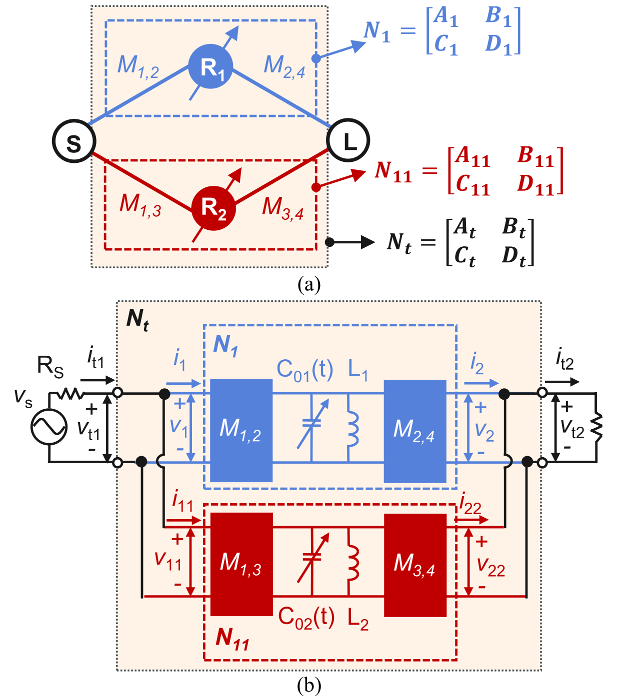

Fig. 1. STM doublet concept. (a) Coupling routing diagram. Colored circles with arrows: STM resonators, white circles: non-resonating nodes. (b) Equivalent circuit where the STM resonators are representd by time-varying capacitors and time-invariant inverters and inductors. N_t, N_1 and N_{11} are the ABCD matrices of the doublet, the upper transversal path and the bottom transversal path.

the resonator R_x) are time invariant. C_{0x} is the nominal (dc) capacitance, ξ_x is the modulation depth, f_m is the modulation frequency, and ϕ_x is the phase of the modulating waveform of the resonator R_x.

$$C_{0x}(t) = C_{0x} + \xi_x C_{0x} \cos(2\pi f_m t + \phi_x) \tag{1}$$

The spectral admittance matrices $\mathbf{Y_{Cx}}$ and $\mathbf{Y_{Lx}}$ for the shunt time-varying capacitor and the time-invariant inductor are provided in (2), as shown at the bottom of the next page. These matrices incorporate the energy conversion between different intermodulation frequencies $f \pm n f_m (n = 0, 1, 2)$ [13], [30]. As such, they should have theoretically infinite dimensions (i.e., n is infinite), but only a limited number of intermodulation frequencies need to be considered in practice. Using the expressions in (1) and (2), the ABCD matrix of a single time-varying resonator $\mathbf{N_{Rx}}$ and a time-invariant inverter $\mathbf{N_{Ma,b}}$ can be calculated using (3) and (4), where a and b are the indices of the inverters, $\mathbf{U}$ is the unity matrix and $\mathbf{0}$ is the zero matrix with the same dimension as the spectral admittance matrices $\mathbf{Y_{Cx}}$ and $\mathbf{Y_{Lx}}$. Since the blue and the red parts are the cascade connection of three two-port networks, $\mathbf{N_1}$ and $\mathbf{N_{11}}$ can be easily found by multiplying the ABCD matrices of the individual two-port subnetworks as shown in (5) and (6), respectively [31]. $\mathbf{N_t}$ can be derived from $\mathbf{N_1}$ and $\mathbf{N_{11}}$ by considering the signal relations in (7)-(10) and its matrix elements are provided in (11)-(14). They have been obtained by substituting (7) and (8) in the relationships outlined in (9) and (10) that lead to $\mathbf{V_{t1}}$, $\mathbf{V_{t2}}$, $\mathbf{I_{t1}}$ and $\mathbf{I_{t2}}$, which can be used to calculate the ABCD elements of $\mathbf{N_t}$.

The S-parameters of the transversal cell $\mathbf{S_t}$ can be calculated from $\mathbf{N_t}$ using (15), as shown at the bottom of the page, where $\mathbf{S_{11}}$, $\mathbf{S_{21}}$, $\mathbf{S_{12}}$ and $\mathbf{S_{22}}$ represent the elements in $\mathbf{S_t}$ and A, B, C and D are the elements of $\mathbf{N_t}$ as provided in [13].

$$\mathbf{N_{Rx}} = \begin{bmatrix} \mathbf{A_{Rx}} & \mathbf{B_{Rx}} \\ \mathbf{C_{Rx}} & \mathbf{D_{Rx}} \end{bmatrix} = \begin{bmatrix} \mathbf{U} & \mathbf{0} \\ \mathbf{Y_{Lx}} + \mathbf{Y_{Cx}} & \mathbf{U} \end{bmatrix} \tag{3}$$

$$\mathbf{N_{M_{a,b}}} = \begin{bmatrix} \mathbf{A_{M_{a,b}}} & \mathbf{B_{M_{a,b}}} \\ \mathbf{C_{M_{a,b}}} & \mathbf{D_{M_{a,b}}} \end{bmatrix} = \begin{bmatrix} \mathbf{0} & \frac{\mathbf{j}}{\mathbf{M_{a,b}}}\mathbf{U} \\ \mathbf{jM_{a,b}U} & \mathbf{0} \end{bmatrix} \tag{4}$$

$$\mathbf{N_1} = \mathbf{N_{M_{1,2}}} \times \mathbf{N_{R1}} \times \mathbf{N_{M_{2,4}}} \tag{5}$$

$$\mathbf{N_{11}} = \mathbf{N_{M_{1,3}}} \times \mathbf{N_{R2}} \times \mathbf{N_{M_{3,4}}} \tag{6}$$

$$\boldsymbol{V_1} = \boldsymbol{A_1 V_2} + \boldsymbol{B_1 I_2}, \quad \boldsymbol{V_{11}} = \boldsymbol{A_{11} V_{22}} + \boldsymbol{B_{11} I_{22}} \tag{7}$$

$$\boldsymbol{I_1} = \boldsymbol{C_1 V_2} + \boldsymbol{D_1 I_2}, \quad \boldsymbol{I_{11}} = \boldsymbol{C_{11} V_{22}} + \boldsymbol{D_{11} I_{22}} \tag{8}$$

$$\boldsymbol{V_{t1}} = \boldsymbol{V_1} = \boldsymbol{V_{11}}, \quad \boldsymbol{V_{t2}} = \boldsymbol{V_2} = \boldsymbol{V_{22}} \tag{9}$$

$$\boldsymbol{I_{t1}} = \boldsymbol{I_1} + \boldsymbol{I_{11}}, \quad \boldsymbol{I_{t2}} = \boldsymbol{I_2} + \boldsymbol{I_{22}} \tag{10}$$

$$\mathbf{A_t} = (\mathbf{B_1^{-1}} + \mathbf{B_{11}^{-1}})^{-1} \left(\mathbf{B_1^{-1} A_1} + \mathbf{B_{11}^{-1} A_{11}}\right) \tag{11}$$

$$\mathbf{B_t} = (\mathbf{B_1^{-1}} + \mathbf{B_{11}^{-1}})^{-1} \tag{12}$$

$$\mathbf{C_t} = \mathbf{C_1} + \mathbf{C_{11}} + (\mathbf{D_1} - \mathbf{D_{11}})(\mathbf{B_1} + \mathbf{B_{11}})^{-1}(\mathbf{A_{11}} - \mathbf{A_1}) \tag{13}$$

$$\mathbf{D_t} = \mathbf{D_{11}} + (\mathbf{D_1} - \mathbf{D_{11}})(\mathbf{B_1} + \mathbf{B_{11}})^{-1}\mathbf{B_{11}} \tag{14}$$

Once the ABCD and scattering matrices of a single STM two-resonator transversal cell are obtained, the scattering matrices of filtering topologies based on STM transversal cells becomes a straightforward process, as they can be regarded as the cascading connection between single STM resonators, time-invariant inverters and STM transversal cells.

To evaluate the feasibility of the aforementioned design method for the synthesis of highly-selective filtering transfer functions, four fully-directional filtering topologies (Topology 1-4) are considered. Specifically, Topologies 1 and 2 demonstrate two different ways to realize a 4th order transfer functions by arranging 4 STM resonators

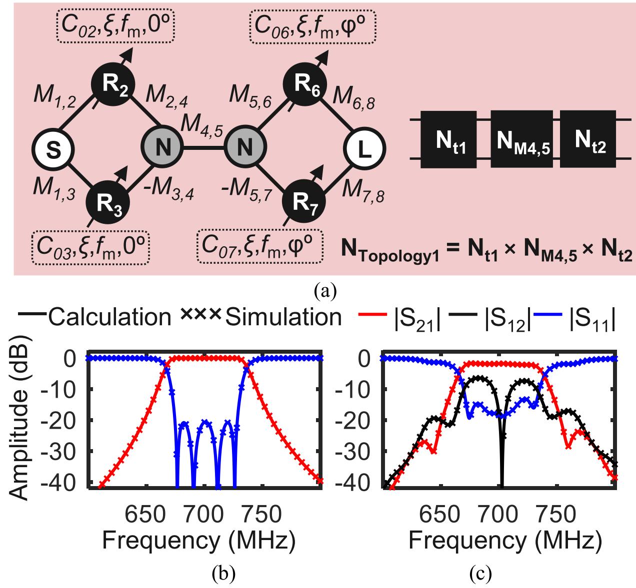

Fig. 2. (a) Topology 1. (b), (c) Synthesized and circuit-simulated S-parameters when STM is OFF (left) and ON (right). The coupling coefficients (obtained by optimization) are $M_{1,2} = M_{2,4} = M_{5,6} = M_{6,8} = M_{1,3} = M_{3,4} = M_{5,7} = M_{7,8} = 0.62$, $M_{4,5} = 1.56$, $M_{2,2} = M_{6,6} = 0.62$, $M_{3,3} = M_{7,7} = -0.67$ and the resonator element values are: $L_r = 2.4$ nH, $C_{02} = C_{06} = 23.06$ pF, $C_{02} = C_{06} = 20$ pF.

in either two cascaded doublets or in a box-like configuration. Furthermore, by adding STM resonators at the input and output ports of the Topology 2 CRD, a sixth order transfer function can be obtained as shown in Topology 3. To facilitate multiple levels of tuning within a single RF filtering configuration, three series-cascaded transversal cells are used as shown in the Topology 4 CRD.

A. Topology 1

The CRD details of the Topology 1 fully-directional STM-based BPF are provided in Fig. 2. In each transversal cell, the two resonators are asynchronously tuned and the inverters

$$\mathrm{Y_{Cx}} = \mathrm{j}2\pi \mathrm{C_x} \begin{bmatrix} f-2f_m & (f-2f_m)\frac{\xi_x}{2}\mathrm{e}^{-\mathrm{j}\phi_x} & 0 & 0 & 0 \\ (f-f_m)\frac{\xi_x}{2}\mathrm{e}\phi_x & f-f_m & (f-f_m)\frac{\xi_x}{2}\mathrm{e}^{-\mathrm{j}\phi_x} & 0 & 0 \\ 0 & f\frac{\xi_x}{2}\mathrm{e}^{\mathrm{j}\phi_x} & f & f\frac{\xi_x}{2}\mathrm{e}^{-\mathrm{j}\phi_x} & 0 \\ 0 & 0 & (f+f_m)\frac{\xi_x}{2}\mathrm{e}^{\mathrm{j}\phi_x} & f+f_m & (f+f_m)\frac{\xi_x}{2}\mathrm{e}^{-\mathrm{j}\phi_x} \\ 0 & 0 & 0 & (f+2f_m)\frac{\xi_x}{2}\mathrm{e}\phi_x & f+2f_m \end{bmatrix}$$

$$\mathrm{Y_{Lx}} = 1/\mathrm{j}2\pi \mathrm{L_x} \begin{bmatrix} f-2f_m & 0 & 0 & 0 & 0 \\ 0 & f-f_m & 0 & 0 & 0 \\ 0 & 0 & f & 0 & 0 \\ 0 & 0 & 0 & f+f_m & 0 \\ 0 & 0 & 0 & 0 & f+2f_m \end{bmatrix} \tag{2}$$

$$\begin{bmatrix} S_{11} & S_{12} \\ S_{21} & S_{22} \end{bmatrix} = \begin{bmatrix} U - 2\left[U + (AR_L + B)(CR_SR_L + DR_S)^{-1}\right]^{-1} & 2\left[U + (AR_L + B)(CR_SR_L + DR_S)^{-1}\right]^{-1} \times \\ 2\sqrt{\frac{R_S}{R_L}}\left[A + \frac{B}{R_L} + CR_S + D\frac{R_S}{R_L}\right]^{-1} & \left[A - (AR_L + B)(CR_L + D)^{-1}C\right] \\ \sqrt{2} & U - 2\left[U + (AR_L + CR_SR_L)^{-1}(B + DR_S)\right]^{-1} \end{bmatrix} \tag{15}$$

$M_{3,4}$ and $M_{5,7}$ need to have opposite polarity to obtain a four-pole bandpass transfer function. All the STM resonators (denoted by the black circles) consist of a parallel time-invariant inductor with the same inductance L_r and time-varying capacitors, whose capacitance are labeled in the boxes next to them. Specifically, all the time-varying capacitors have a nominal capacitance C_{0x}, and have the same modulation frequency f_m and modulation depth ξ. To enable directionality, the phase arrangement for the capacitors should follow the configuration labeled in the figure, i.e., 0° for R_2 and R_3 and φ° for R_6 and R_7. For analysis purposes, the Topology 1 S-parameters can be calculated from its overall ABCD matrix that is equal to $\mathbf{N_{t1}} \times \mathbf{N_{M4,5}} \times \mathbf{N_{t2}}$ where $\mathbf{N_{t1}}$ is the ABCD matrix of the first doublet, $\mathbf{N_{M4,5}}$ is the ABCD matrix of the inverter and $\mathbf{N_{t2}}$ is the ABCD matrix of the last doublet.

For validation purposes, the synthesized S-parameters of Topology 1 are compared with their corresponding circuit-simulated ones (obtained in ADS from Keysight, utilizing ideal LC components and non-linear capacitors with the time-varying capacitance) and are provided in Figs. 2(b) and 2(c) using the element values in the caption of Fig. 2 and considering an intermodulation index of 4 (intermodulation frequencies $f \pm nf_m$ ($n = 0, 1, 2, 3, 4$) is considered). It should be noted that the coupling element values have been obtained by optimization. As shown, the BPF works at 700 MHz with a fractional BW of 10%. Furthermore, as observed in Figs. 2(b), when STM is OFF ($\xi = 0$), the filter response is reciprocal, i.e., $|S_{21}| = |S_{12}|$. When STM is ON ($\xi \neq 0$), really high IS can be created between the forward and backward transmission directions, as shown in Fig. 2(c). Moreover, a strong agreement between the synthesized results and the circuit simulated results can be observed, indicating the validity of the proposed synthesis method using STM transversal cells.

The tuning capabilities of Topology 1 are examined in Fig. 3 through various design cases. As shown in Fig. 3(a), the center frequency of the filter can be tuned to lower (higher) frequencies by increasing (decreasing) the capacitance of all the four resonators at the same time whilst preserving high isolation between the forward and the backward direction. The BW tuning capabilities of the NR-BPF are presented in Fig. 3(b). Wider (narrower) BW can be achieved by increasing (decreasing) the value of C_{02} and C_{06} while decreasing (increasing) the value of C_{03} and C_{07}. Furthermore, as shown in Case 4 in Fig. 3(b), the BPF can be intrinsically-switched off when C_{02}, C_{06}, C_{03} and C_{07} have the same value. For all of these cases the component element values are provided in the caption of Figs. 2, 3. It is noted that the parameters of the time-varying capacitors should be adjusted accordingly in different tuning stages to achieve optimal isolation levels.

B. Topology 2

The details of the Topology 2 CRD are provided in Fig. 4. It demonstrates an alternative way to functionalize a fourth order transfer function by connecting two synchronously tuned resonators R_2 and R_5, directly to a single transversal cell, forming a box-like topology. A single-band bandpass transfer function can be obtained when resonators R_2 and R_5 are set

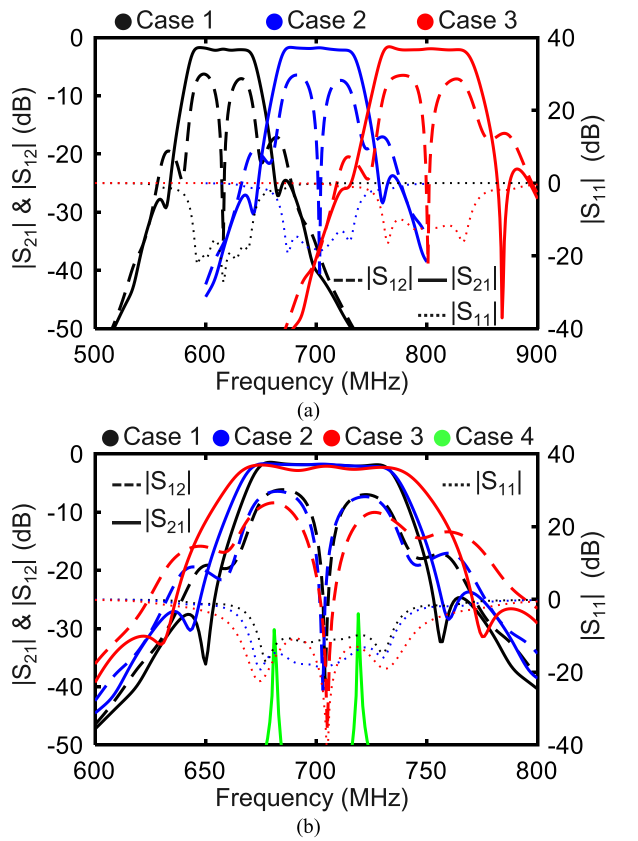

Fig. 3. Circuit–simulated tuning capabilities for Topology 1. (a) Center frequency tuning. The parameters are: Case 1: $C_{02} = C_{06} = 30.05$ pF, $C_{03} = C_{07} = 26.04$ pF, $f_m = 26$ MHz, $\xi = 0.068, \varphi = 53$; Case 2: $C_{02} = C_{06} = 23.06$ pF, $C_{03} = C_{07} = 20$ pF, $f_m = 30$ MHz, $\xi = 0.067, \varphi = 53$; Case 3: $C_{02} = C_{06} = 15.44$ pF, $C_{03} = C_{07} = 20$ pF, $f_m = 30$ MHz, $\xi = 0.067, \varphi = 53$. (b) BW tuning. The parameters are: Case 1: $C_{02} = C_{06} = 22.74$ pF, $C_{03} = C_{07} = 20.1$ pF, $f_m = 26.5$ MHz, $\xi = 0.061$, $\varphi = 53$; Case 2: $C_{02} = C_{06} = 23.06$ pF, $C_{03} = C_{07} = 20$ pF, $f_m = 30$ MHz, $\xi = 0.067$, $\varphi = 53$; Case 3: $C_{02} = C_{06} = 23.46$ pF, $C_{03} = C_{07} = 19.56$ pF, $f_m = 33$ MHz, $\xi = 0.088$, $\varphi = 74$. Case 4: $C_{02} = C_{06} = C_{03} = C_{07} = 21.54$ pF, $\xi = 0$, $\varphi = 60$.

to resonate at the center frequency of the BPF, while R_3 and R_4 resonate at lower and higher frequencies. Using as a basis the design methodology mentioned above, a fourth order BPF was designed at 700 MHz with a fractional BW of 9% using the parameters specified in the captions of Fig. 4 (coupling element values have been obtained by optimization). Furthermore, R_2 is modulated with an AC signal having a phase of 0°, R_3 and R_4 with an AC signal having a phase of φ° and R_5 with a phase of 2φ°. Figs. 4(b) and 4(c) demonstrate a comparison between the synthesized S-parameters and the ones obtained by circuit simulations which appear to be in excellent agreement. The tuning capabilities of Topology 2 are shown in Fig. 5 in terms of center frequency (Fig. 5(a), Case 1-3), BW tuning (Fig. 5(b), Case 1-3)) and intrinsic switching off (Fig. 5(b), Case. 4). They were obtained in a similar manner to the ones of Topology 1.

C. Topology 3

The Topology 3 CRD in Fig. 6 demonstrates scalability to higher-order transfer functions by cascading two additional resonators in the box-like Topology 2 configuration, resulting in a sixth-order single-band bandpass transfer function.

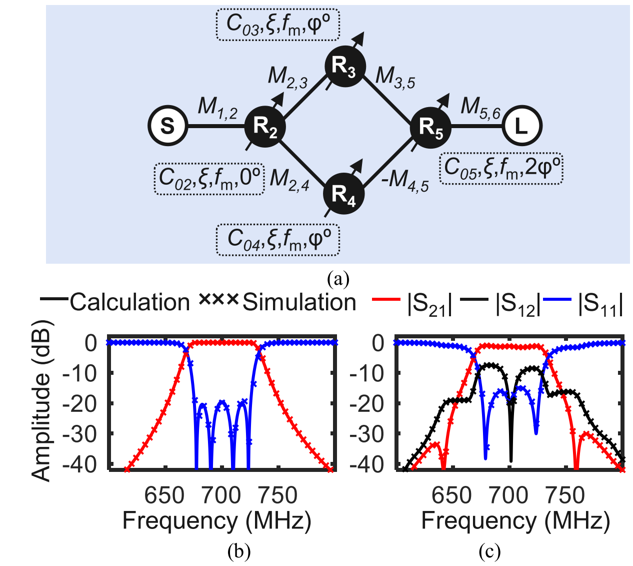

Fig. 4. (a) Topology 2. (b), (c) Synthesized and circuit-simulated S-parameters of Topology 2 when STM is OFF (left) and OFF (right). The coupling coefficients obtained by optimization are $M_{1,2} = M_{5,6} = 0.936$, $M_{2,3} = M_{3,5} = M_{2,4} = M_{4,5} = 0.52$, $M_{2,2} = M_{5,5} = 0$, $M_{3,3} = 0.562$, $M_{4,4} = -0.562$ and the resonator element values are: $L_r = 7.74$ nH, $C_{02} = C_{05} = 6.68$ pF, $C_{03} = 7.02$ pF, $C_{04} = 6.35$ pF.

As depicted in Fig. 6(a), to achieve directionality, the modulating AC signals need to be applied with the following phase progression: 0° for the signal applied to R_2, $\varphi°$ for R_3, $2\varphi°$ for R_4 and R_5, $3\varphi°$ for R_6, and $4\varphi°$ for R_7. The comparison between the synthesized S-parameters and the circuit-simulated ones is presented in Figs. 6(b) and 6(c). They have been obtained with the same method as above and appear to be in an excellent agreement, successfully validating the proposed synthesis method. The tuning capabilities of Topology 3 are similar to the ones obtained for Topology 2, thus omitted here for brevity.

D. Topology 4

Topology 4 facilitates the realization of multi-functional/configurable transfer functions by only tuning the resonant frequencies of its constituent resonators. Specifically, it enables various levels of tunability, such as center frequency, bandwidth, intrinsic switching off, reconfigurability of the number of passbands through band merging and cancellation and tuning of the out-of-band rejection by transmission zero (TZ) reallocation. To achieve these functionalities, all inverters share the same polarity, and the phases of the two resonators within the same STM transversal cell are identical. However, a successive phase difference is required for adjacent transversal cells, as illustrated in Fig. 7.

A summary of the tuning capabilities of Topology 4 is provided in Fig. 8, using the component element values in the caption and in Table I. The coupling coefficients for all 6 tuning states are the same as listed in Fig.7. As shown in Fig. 8(a), a third order dual-band transfer function can be generated when resonators R_2, R_6 and R_{10} are set to the same frequency that coincides with that of the higher passband while resonators R_3, R_7 and R_{11} resonate at the lower passband. In another configuration [see Case 2 in Fig. 8(b)],

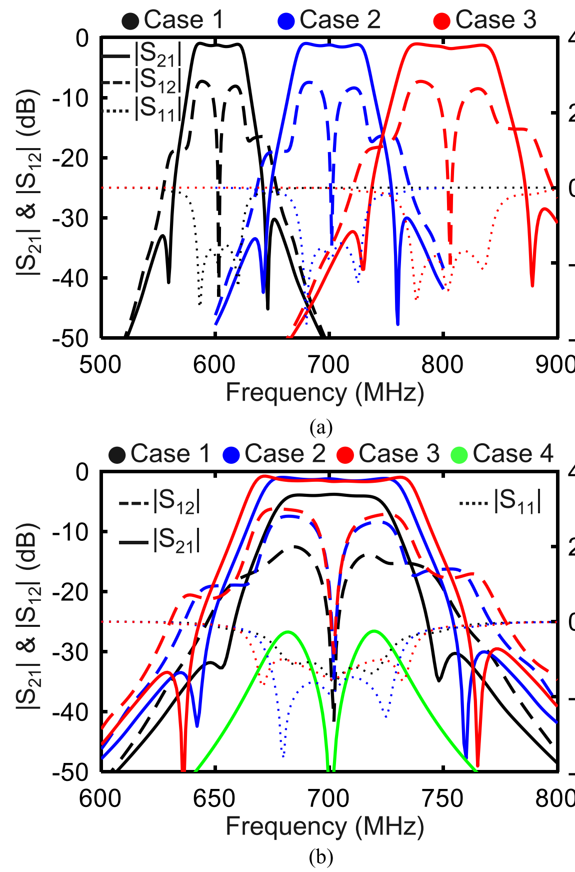

Fig. 5. Circuit–simulated tuning capabilities for Topology 2. (a) Center frequancy tuning. The parameters are: Case 1: $C_{02} = C_{05} = 9.035$ pF, $C_{03} = 9.43$ pF, $C_{04} = 8.65$pF, $f_m = 22$ MHz, $\xi = 0.055$, $\varphi = 60$; Case 2: $C_{02} = C_{05} = 6.68$ pF, $C_{03} = 7.02$ pF, $C_{04} = 6.35$ pF, $f_m = 30$ MHz, $\xi = 0.065$, $\varphi = 60$; Case 3: $C_{02} = C_{05} = 5.08$ pF, $C_{03} = 5.38$ pF, $C_{04} = 4.8$ pF, $f_m = 37$ MHz, $\xi = 0.073$, $\varphi = 60$; (b) BW tuning. The parameters are: Case 1: $C_{02} = C_{05} = 6.68$ pF, $C_{03} = 6.848$ pF, $C_{04} = 6.497$ pF, $f_m = 23.5$ MHz,$\xi = 0.06$, $\varphi = 60$; Case 2: $C_{02} = C_{05} = 6.68$ pF, $C_{03} = 7.02$ pF, $C_{04} = 6.35$ pF, $f_m = 30$ MHz, $\xi = 0.065$, $\varphi = 60$; Case 3: $C_{02} = C_{05} = 6.68$ pF, $C_{03} = 7.151$ pF, $C_{04} = 6.26$ pF, $f_m = 32$ MHz, $\xi = 0.065$, $\varphi = 60$; Case 4: $C_{02} = C_{05} = C_{03} = C_{04} = 6.68$ pF, $f_m = 30$ MHz, $\xi = 0$, $\varphi = 60$.

TABLE I
PARAMETERS FOR TIME-VARYING CAPACITANCE FOR THE DIFFERENT TUNING CASES OF FIG.8

	1	**2**	**3**	**4**	**5**	**6**
C_{02} (pF)	20.236	21.5	15.6	15.5	15.5	18.055
C_{03} (pF)	23	21.5	21.5	21.5	21.5	26.552
C_{06} (pF)	20.236	21.5	14.6	21.5	21.5	22.1
C_{07} (pF)	23	21.5	21.5	21.5	21.5	22.02
C_{010} (pF)	20.236	21.5	26.6	30.7	21.5	7.568
C_{011} (pF)	23	21.5	21.5	21.5	21.5	63.73
f_m(MHz)	20	33	19.5	21	24	20
ξ	0.05	0.085	0.052	0.053	0.07	0.05
φ(°)	65	65	65	65	65	65

an equi-ripple response can be generated by setting all the resonators to resonate at the same frequency. Furthermore,

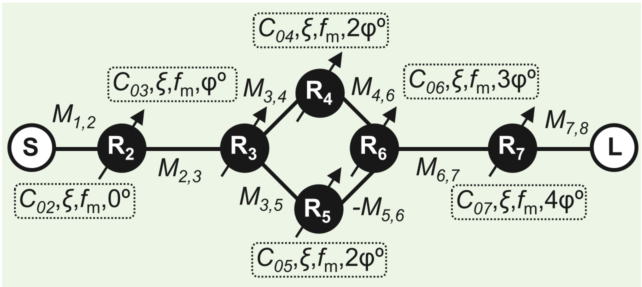

(a)

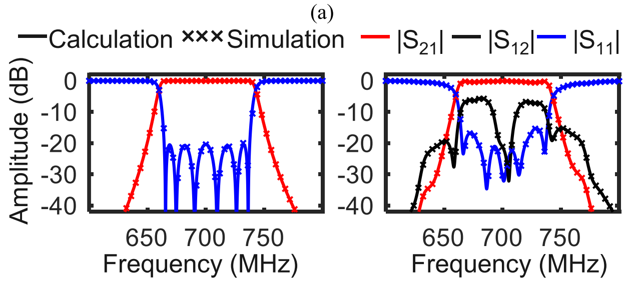

(b) (c)

Fig. 6. (a) Topology 3. (b), (c) Synthesized and circuit-simulated S-parameters of Topology 3 when STM is OFF (left) and ON (right). The coupling coefficients are obtained by optimization and are $M_{1,2} = M_{7,8} = 0.769$, $M_{2,3} = M_{6,7} = 0.484$, $M_{3,4} = M_{4,6} = M_{3,5} = M_{5,6} = 0.244$, $M_{2,2} = M_{3,3} = M_{6,6} = M_{7,7} = 0$, $M_{4,4} = 0.356$, $M_{5,5} = -0.326$ and the resonator element values are: $L_r = 6$ nH, $C_{02} = C_{03} = C_{06} = C_{07} = 8.6$ pF, $C_{04} = 9.16$ pF, $C_{05} = 8.1$ pF.

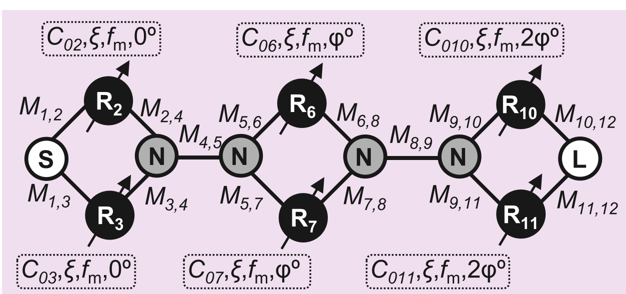

Fig. 7. Topology 4. The coupling coefficients (obtained by optimization) are $M_{1,2} = M_{5,6} = M_{6,8} = M_{10,12} = 0.837$, $M_{1,3} = M_{5,7} = M_{7,8} = M_{11,12} = 0.86$, $M_{2,4} = M_{9,10} = 1$, $M_{3,4} = M_{9,11} = 1.028$, $M_{8,9} = M_{4,5} = 1.364$, and the resonator inductances are: $L_r = 2.4$ nH.

when placing three resonators inside the passband (resonators R_3, R_7 and R_{11}), and the rest are outside of the passband, transfer functions with three transmission zeros (TZs) can be generated, as demonstrated in Fig. 8(c). Figs. 8(d) and 8(e) show the transfer functions that can be obtained when placing resonators R_3, R_6, R_7 and R_{11} inside the passband, facilitating quasi-elliptic transfer functions with two symmetrically allocated TZs around the passband or with just one TZ. The filter can also be intrinsically switched-off [see Case 6 in Fig. 8(f)] when setting resonators R_6 and R_7 to resonate at the same frequency while offsetting the other resonators from the center frequency of the filter. Although not shown here, the center frequency in all the aforementioned cases can be freely tuned through altering all the resonators' resonating frequency at the same time as it will be shown in the experimental validation of this concept. Furthermore, the zeros in Cases 3 to 5 can be placed at either side of the passband. Their location can be altered by tuning the corresponding resonators. As can be observed from Fig. 8, large isolation levels can be achieved in all the tuning states, demonstrating the effectiveness and versatility of the proposed topologies.

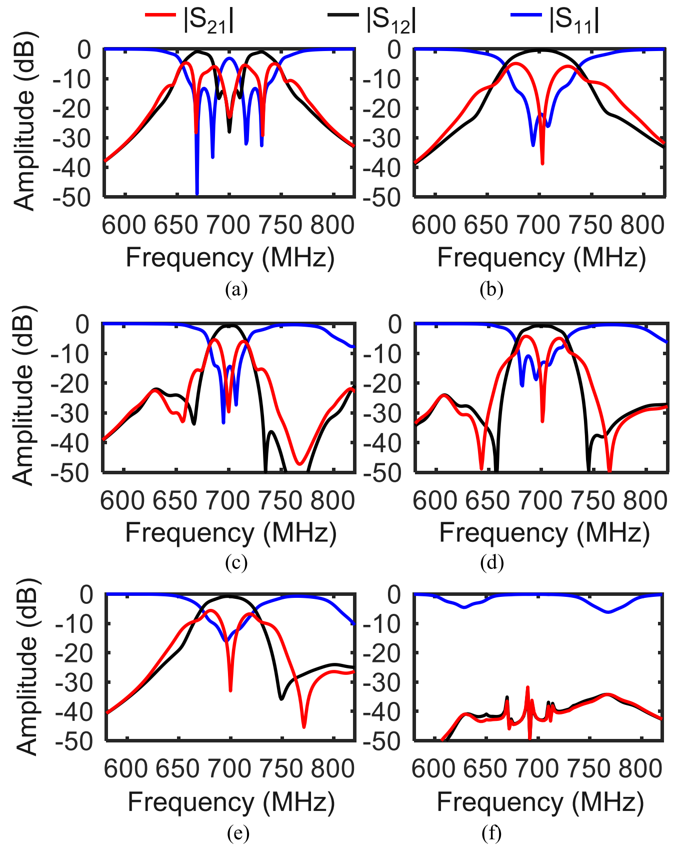

Fig. 8. Circuit-simulated tuning capabilities of Topology 4 using the component values in Table I. (a) Case 1, (b) Case 2, (c) Case 3, (d) Case 4, (e) Case 5, (f) Case 6.

III. STM Parameters Selection And Practical Realization Aspects

A. STM Parameters Selection

Directionality in the transversal-based BPFs can be achieved when the capacitance of the constituent resonators follows the sinusoidal variation described in (1). Depending on the selected modulation parameters ξ, f_m and φ, alternative S-parameter profiles can be obtained. Thus, parametric studies need to be performed to determine the desired transfer function characteristics as shown for the example cases of Topology 1 and Topology 4 in Figs. 9 and 10. Similar studies can be performed for the rest of the filtering topologies, but they have been omitted for brevity. In order to effectively present the parametric sweeping results, two data visualization methods have been adopted, namely line plots and heatmaps. These two complementary data visualization techniques provide a comprehensive view of the parametric sweeping results, and their characteristics are summarized as follows:

1. Line plots [Figs. 9(a) and 10(a)]: In these figures, the amplitudes of the S-parameters ($|S_{11}|$, $|S_{21}|$, and $|S_{12}|$) along with the directivity ($D = |S_{21}|$-$|S_{21}|$) are plotted on the y-axis against frequency on the x-axis. Curves representing different modulation parameters are plotted in the same coordinate

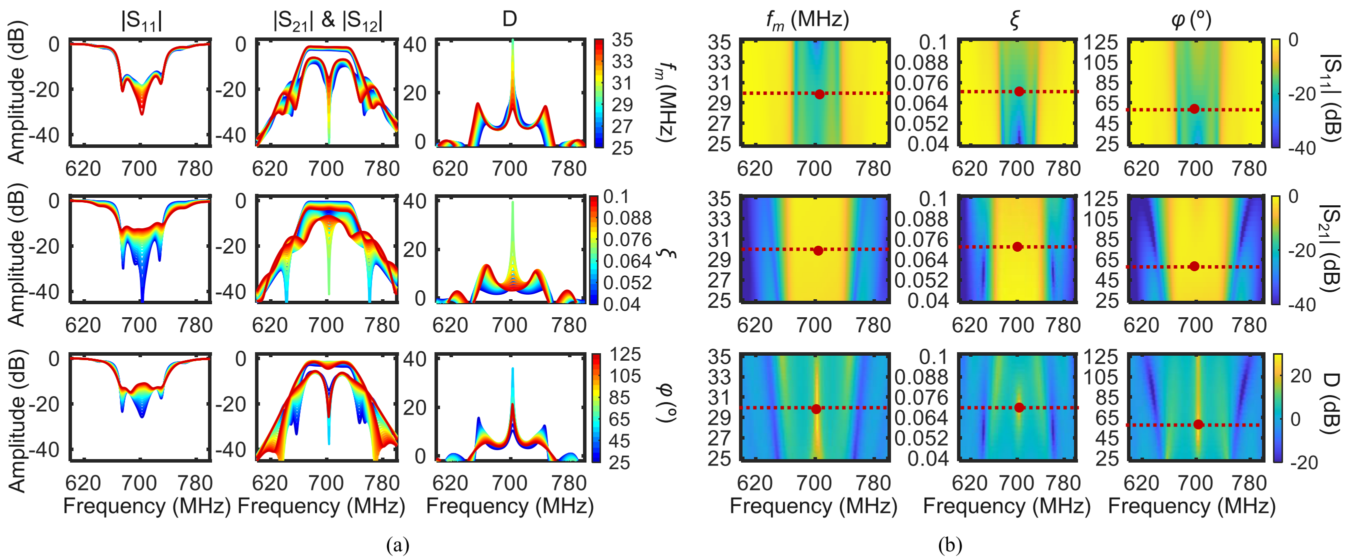

Fig. 9. S-parameters of Topology 1 when varying f_m, ξ and φ. (a) Line plots. (b) Heatmap plots.

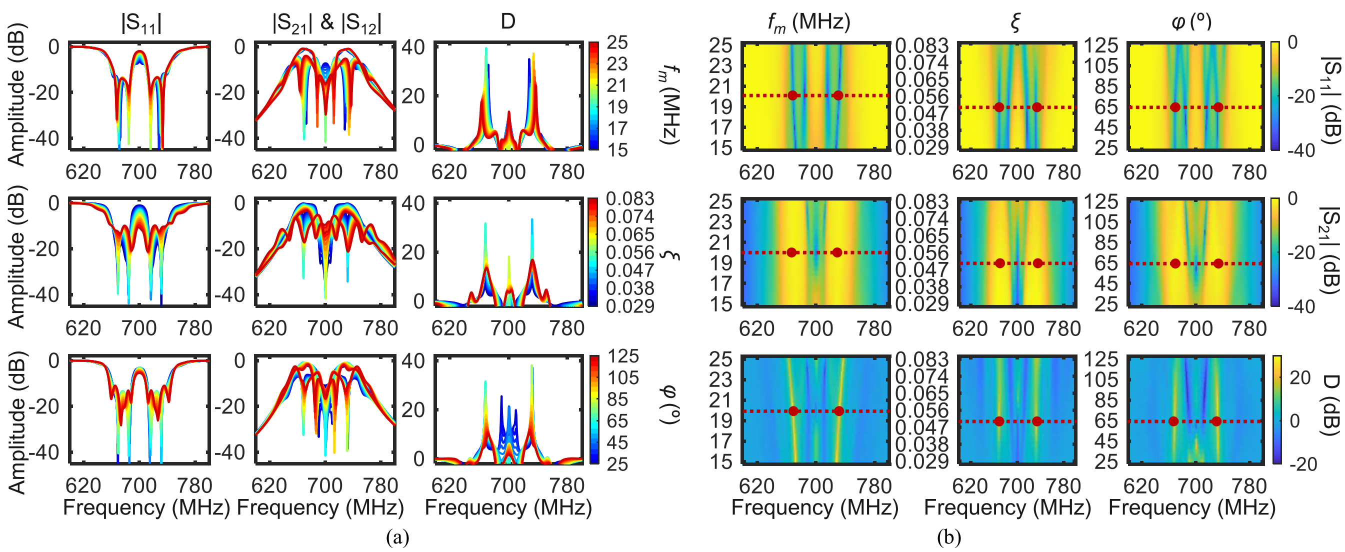

Fig. 10. S-parameters of Topology 4 operating in the dual band mode when varying f_m, ξ and φ. (a) Line plots. (b) Heatmap plots.

system using varying colors, as indicated by the color bar on the right side of each row. This visualization method allows for convenient observation of how the S-parameter shapes change with the modulation parameters.

2. Heatmaps [Figs. 9(b) and 10(b)]: These figures employ a heatmap approach to display the S-parameters as colors in a two-dimensional matrix. One axis represents the frequency range, while the other axis represents the modulation parameters. The color intensity in each cell indicates the value of the corresponding S-parameter.

Using as a basis these performance visualization methods, the Topology 1 performance trade-off metrics are provided in Fig.9. Specifically, a $f_m = 30$ MHz results in the highest D and an acceptable insertion loss (IL). Larger f_m values lead to lower IL but also lower D, while too small f_m values lead to high IL and low D as well. Regarding the modulation index ξ, the optimal value is chosen when $\xi = 0.07$. Although lower ξ values yield lower IL, the D is also lower. Too high ξ values cause both lower D and higher IL. Finally, an optimal value of 60° can be observed for φ, which achieves high directivity with low IL while maintain good transfer function shapes. Fig. 10 illustrates the trade-offs analysis study for Topology 4 when operating in a dual-band mode of operation. The optimal modulation parameters of the dual-band BPF are chosen as $f_m = 20$ MHz, $\xi = 0.05$ and $\varphi = 65°$ for high D for both bands while maintain an acceptable IL and good transfer function shapes. Using as a reference these plots, optimal STM parameters can be selected for the desired S-parameters for Topology 1 and 4 and are demonstrated in Figs. 3(b) and 3(h), respectively.

B. Practical Realization Aspects

1) Lumped–Element-Based Implementation Method: Based on the CRDs and the coupling coefficients provided in the previous sections, the four multi-functional filtering topologies can be implemented using LEs and conventional filter design techniques to specify the LE element values as for example the ones described in [32]. Next, the DC biasing on the varactor

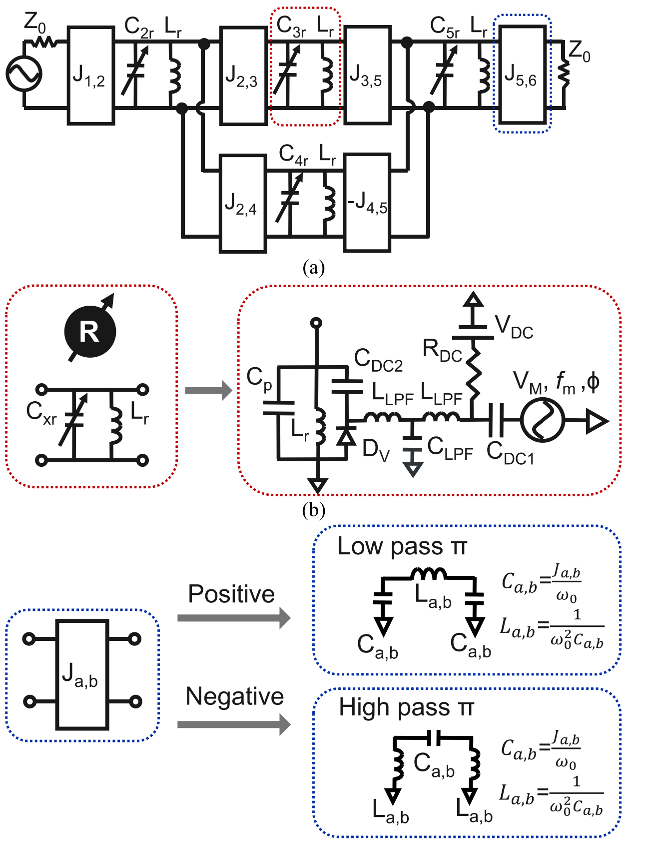

Fig. 11. (a) Circuit equivalent of the CRD in Fig.4 (a). (b) STM resonator implementation using lumped components. (c) Inverter implementation using lumped components.

is selected so that it gives the desired resonator capacitance. Subsequently, the AC modulation parameters f_m, V_M, and ϕ are obtained through parametric simulations according to the desired IL in the forward direction and the desired IS in the reverse direction. Lastly, the tuning capabilities are obtained by altering the DC and AC biasing.

Fig. 11 shows a design example when implementing the CRD of Topology 2 in Fig. 4(a). Firstly, a reciprocal filter is designed based on the CRD and the coupling coefficients and the equivalent circuit is given in Fig. 11(a), where C_{xr} ($x = 2,3,4,5$) is the capacitance L_r is the inductance of the resonators, and $J_{a,b}$ is the inverter value after impedance scaling and bandpass transformation to a center frequency of ω_0 and a fractional bandwidth of FBW. The values can be calculated using (16). The inductance of the resonators are set to the same value of L_r in our designing cases.

$$\begin{aligned} L_x &= \frac{1}{\omega_0\left(\frac{1}{FBW} - \frac{M_{x,x}}{2}\right)}, \quad C_x = \frac{\left(\frac{1}{FBW} + \frac{M_{x,x}}{2}\right)}{\omega_0}, \\ \omega_x &= \frac{1}{\sqrt{L_x C_x}} \\ J_{1,2} &= M_{1,2}\sqrt{\frac{L_2}{Z_0 L_r}}, \quad J_{5,6} = M_{5,6}\sqrt{\frac{L_2}{Z_0 L_r}} \\ J_{a,b} &= M_{a,b}\sqrt{\frac{L_a L_b}{L_r L_r}}\,(a = 2, 3, 4)\,. \end{aligned} \tag{16}$$

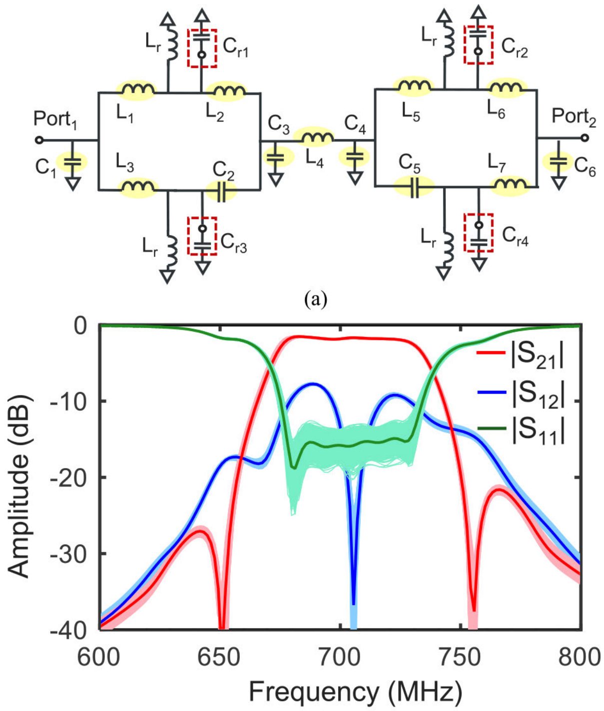

Fig. 12. Sensitivity analysis of Topology 1. (a) Detailed circuit schematic. (b) Monte Carlo simulation results with 1600 iterations and 2% tolerance for the static components marked in yellow when STM is ON.

After acquiring all the parameters of the equivalent circuit in Fig. 11(a), the STM resonators and the static inverters can be implemented using lumped elements as shown in Figs. 11(b) and (c), respectively. Specifically, a parallel inductor L_r, a static capacitor C_r and a varactor diode D_v constitute the inductance and capacitance in each resonator. DC biasing V_{DC} is applied through a 10 MΩ resistor R_{DC} to set the nominal resonant frequency of each resonator. All the resonators are modulated by low frequency AC signals with frequency f_m, amplitude V_m and phase ϕ so that the capacitance of the varactor satisfies the sinusoidal variation as the AC signal applied to it. A low-pass filter is added after each AC source to allow for the modulating AC signals to be applied on the resonators while protecting the AC source from the high frequency RF signals. C_{DC1} and C_{DC2} are used as DC blocks to prevent the DC signals from entering the AC sources and the RF circuit. Positive coupling coefficients are materialized with first order low-pass pi-networks whereas the negative ones with first order high-pass networks as shown in Fig. 11(c) using (17). To reduce the number of circuit elements required, the parallel capacitors of the inverters are combined with the ones of the adjacent resonators.

$$C_{a,b} = \frac{J_{a,b}}{\omega_0}, \quad L_{a,b} = \frac{1}{\omega_0^2 C_{a,b}} \tag{17}$$

2) Sensitivity Analysis: To evaluate the effect of tolerances on the performance of the non-reciprocal RF filtering components, a sensitivity analysis can be conducted for the tolerances which are typically 2%. For the sake of illustration, the circuit architectures of Topology 1 and Topology 2 are analysed through Monte Carlo simulations. The components marked in yellow in Figs. 12(a) and 13(a) are meant to be static and

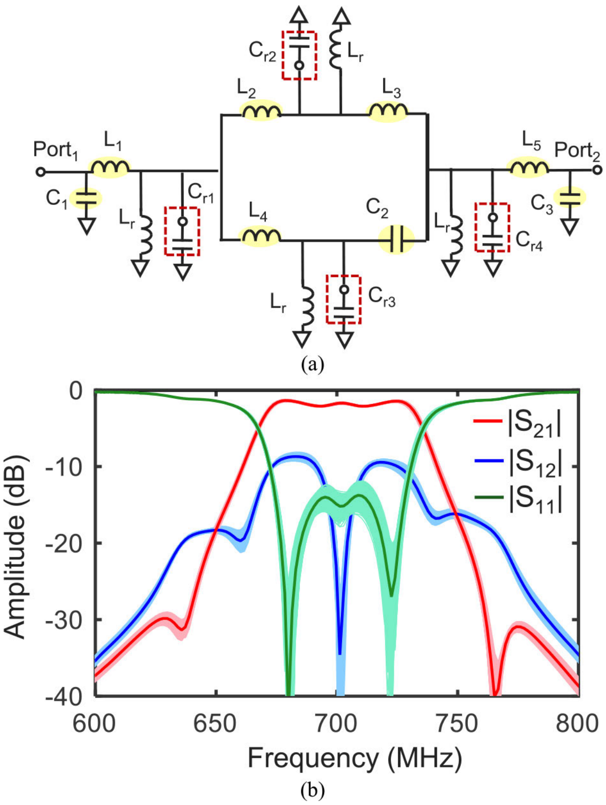

Fig. 13. Sensitivity analysis of Topology 2. (a) Detailed circuit schematic. (b) Monte Carlo simulation results with 1600 iterations and 2% tolerance for the static components marked when STM is ON.

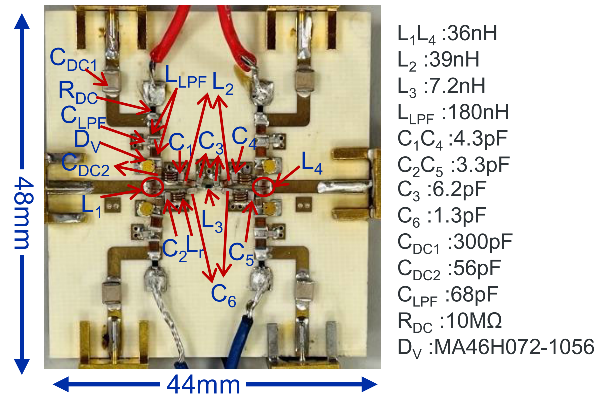

Fig. 14. Manufactured prototype of Filter 1 based on the Toplogy 1 CRD.

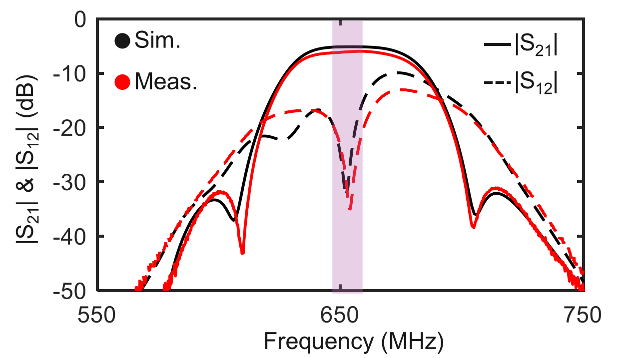

Fig. 15. Comparison of RF-measured and EM-simulated S-parameters for one tuning state of Filter 1. The purple band marks the frequency range when $|S_{12}| < -20$ dB.

as such are chosen to have a 2% tolerance. The simulated results for Topology 1 and Topology 2 are presented in Fig. 12(b) and 13(b), respectively. The solid lines denote the simulation results when all the components have the nominal values while the shaded ones indicate how the S parameters vary with a 2% tolerance for the chosen components in 1600 iterations. It should be noted that for all the 1600 iterations, the same modulation parameters f_m, ξ and φ are adopted. As shown, the effect of the tolerances is almost unnoticeable with the return loss being always below 10 dB and isolation levels remaining >20 dB when STM is turned on.

IV. Experimental Validation

For proof of concept validation purposes of the transversal resonator-based NR-BPF concept, four filter prototypes (Filters 1-4) implementing the CRD Topologies 1-4 were designed, and manufactured on a RO4003C dielectric substrate with a height of 1.5 mm. The S-parameters for the four filters, including their tuning capabilities, were characterized using a Keysight PNA-X N5244A network analyzer.

A. Filter 1

The photograph of the manufactured prototype and the utilized lumped element components are provided in Fig. 14. A comparison of the RF measured and EM simulated S-parameters for one tuning state is shown in Fig. 15. They appear to be in a good agreement successfully validating the proposed concept. The measured 20 dB IS BW (the frequency range when IS> 20 dB) is 647.5 MHz to 659.5 MHz (12 MHz). The frequency band is marked in light purple. The RF measured tuning capabilities for Filter 1 are presented in Fig. 16. Although a finite number of tuning states is shown, the filter exhibits continuous tuning range. Specifically, its center frequency can be tuned between 571 MHz to 724 MHz (1.27) with an insertion loss (IL) ranging from 4.8 dB to 6.5 dB and isolation (IS) between the forward and the backward direction from 21 dB to 33 dB. Fig. 16(b) demonstrates the BW tuning characteristics of the filter which exhibits a tunable BW between 39.5 MHz to 73.9 MHz (1.87) with IL ranging from 5.9 dB to 6.8 dB and IS between its forward and its backward direction between 25 dB to 35 dB. The intrinsic switch-off capability of Filter 1 is also demonstrated in Fig. 16 (b) and is represented by the green traces in Case 4.

B. Filter 2

Fig. 17 depicts the photograph of the manufactured prototype of Filter 2 and a comparison between the RF-measured and the EM-simulated S-parameters for one tuning state are presented in Fig. 18. For this specific tuning state, the measured 20 dB IS BW is 667 MHz to 705 MHz (38.4 MHz). As can be seen from Fig. 19(a), the center frequency of Filter 2 can be tuned between 630 MHz to 735 MHz (1.17). For these states IL varies between 4.8 dB to 6.7 dB and the IS between the forward and the backward direction between 20 dB and 30 dB. Continuous BW tuning between 24.8 MHz to 58.1 MHz (2.34) is shown in Fig. 19(b). For these states,

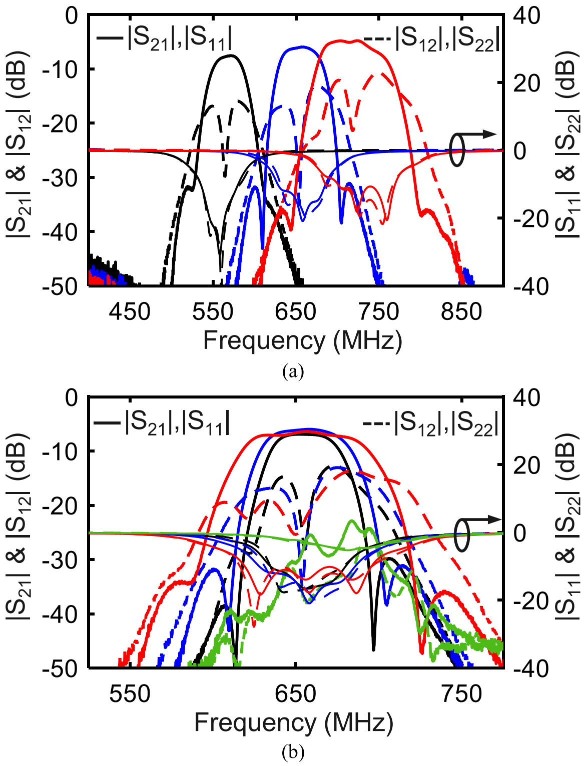

Fig. 16. RF measured tuning capabilities of Filter 1. (a) Center frequency tuning. (b) BW tuning and intrinsic switching-off (green trace).

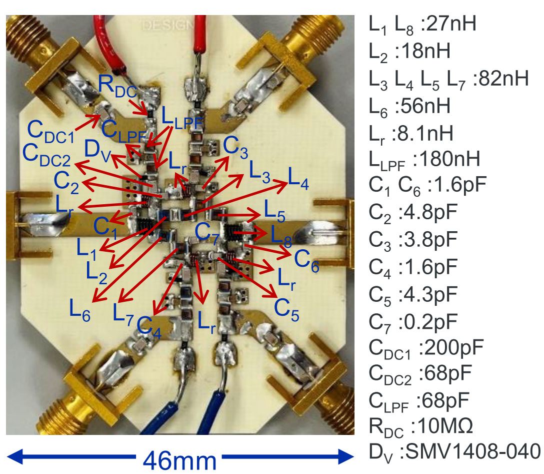

Fig. 17. Manufactured prototype of Filter 2 based on the Topology 2 CRD.

IL varies between 5.4-6.8 dB and the IS between the forward and the backward direction between 29-40 dB. Filter 2 can also be switched-off intrinsically as shown in Case 4 state in Fig. 19(b).

C. Filter 3

The experimental prototype of Filter 3 is provided in Fig. 20. Fig. 21 showcases the good agreement between its EM simulated and RF measured performance for one tuning state further supporting the effectiveness of the transversal resonator-based NR-BPF concept. For this tuning state in Fig. 21, the measured 18 dB IS BW is 670 MHz to 718 MHz (48 MHz). As shown in Fig. 22(a), Filter 3 allows for center

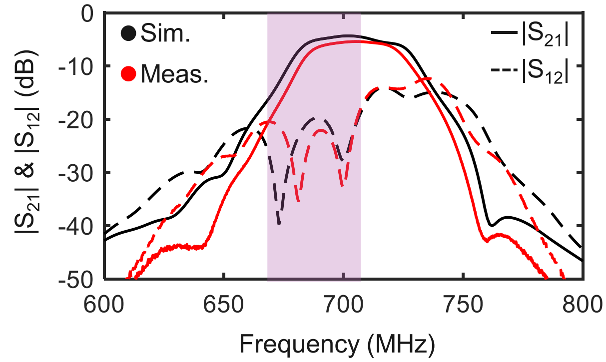

Fig. 18. Comparison of RF measured and EM-simulated S-parameters for one tuning state of Filter 2. The purple band marks the frequency range when $|S_{12}| < -20$ dB.

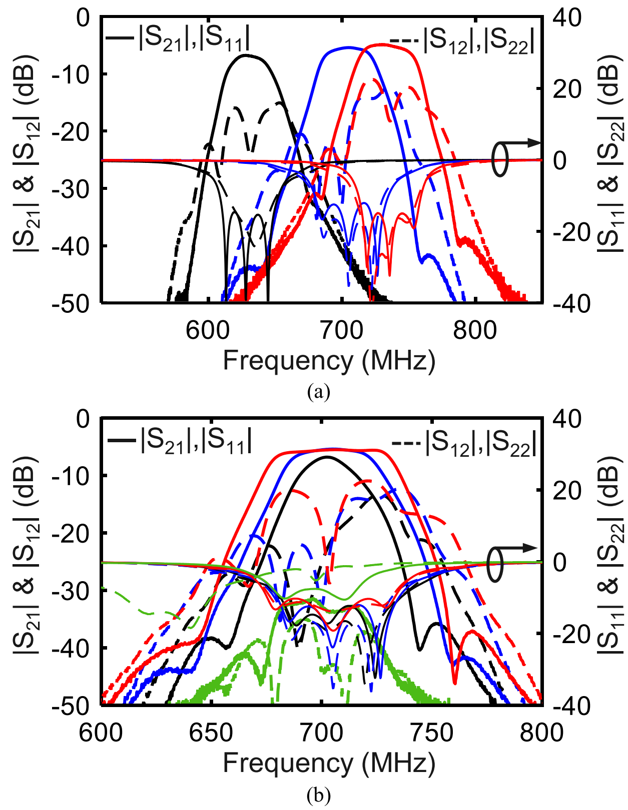

Fig. 19. RF measured tuning capabilities of Filter 2. (a) Center frequency tuning. (b) BW tuning and intrinsic switching-off (green trace).

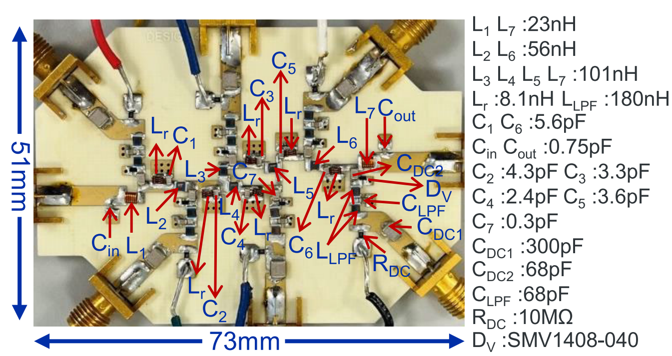

Fig. 20. Manufactured prototype of Filter 3 based on the Topology 3 CRD.

frequency tuning between 655 MHz and 760 MHz (1.16). For these states, the in-band passband IL varies between

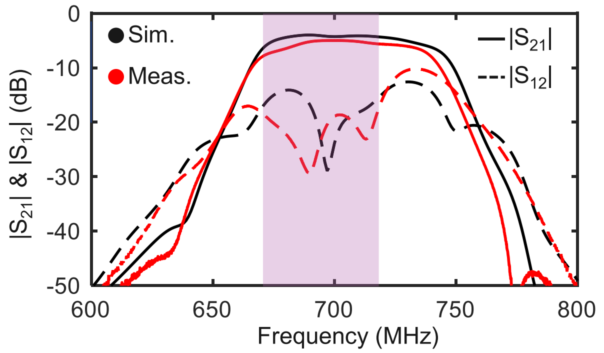

Fig. 21. Comparison of RF measured and EM-simulated S-parameters for Filter 3. The purple band marks the frequency range when $|S_{12}| < -18$ dB.

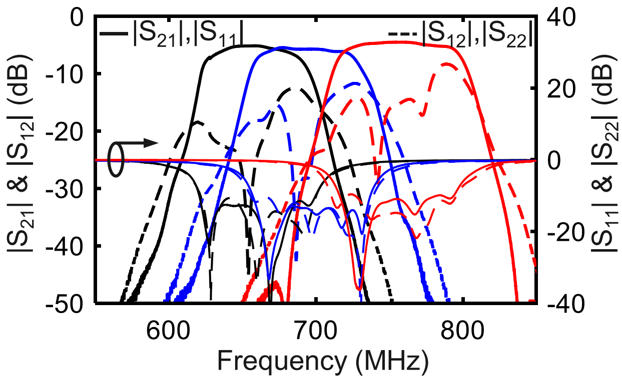

(a)

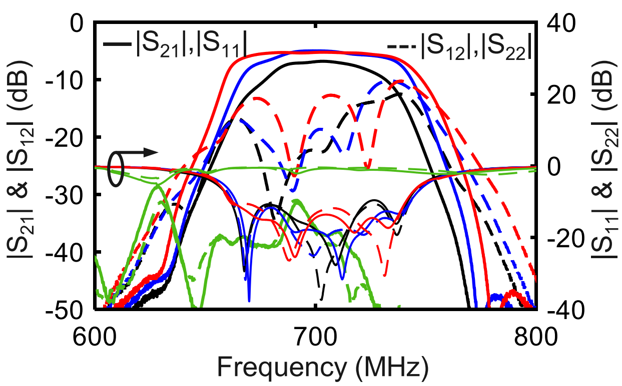

(b)

Fig. 22. RF measured tuning capabilities of Filter 3. (a) Center frequency tuning. (b) BW tuning and intrinsic switching-off (green trace).

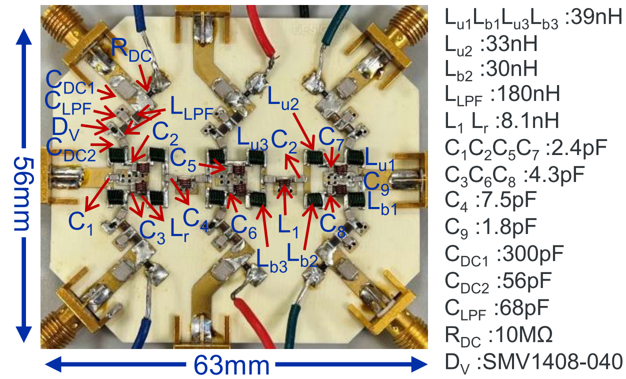

Fig. 23. Manufactured prototype of Filter 4 based on the Topology 4 CRD.

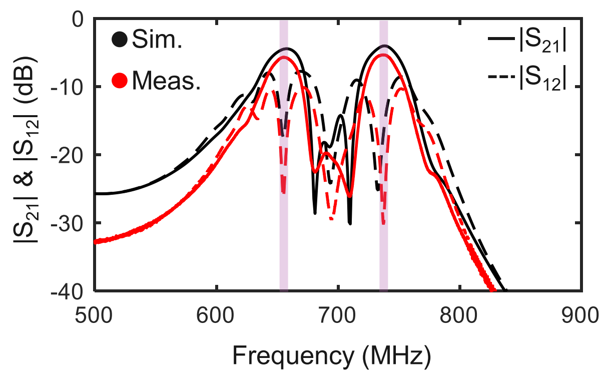

(a)

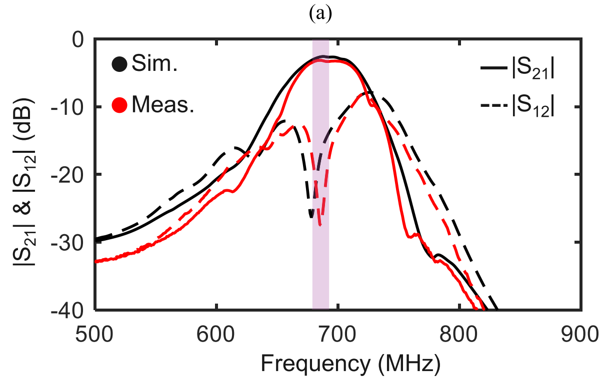

(b)

Fig. 24. Comparison of RF-measured and EM-simulated S-parameters for two example tuning states of Filter 4. The purple band marks the frequency range when $|S_{12}| < -20$ dB. (a) Dual-band state. (b) Single-band state.

4.5 dB and 5.7 dB and the IS between the forward and the backward direction between 30 dB and 45 dB. As illustrated in Fig. 22(b), the BW tuning range of Filter 3 was measured between 52.9 MHz and 84 MHz (1.57), with IL ranging from 4.9 MHZ to 6.7 dB and IS from 27 dB to 34 dB. Filter 3 can also be intrinsically switched-off as demonstrated in Case 4 in Fig. 22.

D. Filter 4

Fig. 23 shows the manufactured prototype of the multi-configurable Filter 4. Figs. 24(a) and 24(b) provide the comparison between the RF-measured and the EM-simulated S-parameters when operating at its dual-band and its single-band mode of operation which appear to be in a good agreement. The measured 20 dB IS BW for the dual-band mode is 653 MHz to 657 MHz (4 MHz) for the lower band and 733 MHz to 740 MHz (7 MHz) for the upper band. The measured 20 dB IS BW for the single-band mode is 681 MHz to 691 MHz (10 MHz). The tuning capabilities of Filter 4 are summarized in Figs. 25 to 26, which show multiple levels of reconfigurability. Specifically, when Filter 4 operates in its single–band mode of operation, the out-of-band response can be reconfigured to have three TZs, two TZs, one TZ and no TZ as shown in Figs. 25 (a)-(d). The center frequency of the four states are 700 MHz and the passband BW is 26 MHz, 34 MHz, 44 MHz and 56 MHz respectively and their in-band IL is 4.46 dB, 3.55 dB, 3.46 dB and 3.2 dB. The measured TFs demonstrate that IS >25 dB can be obtained for all the

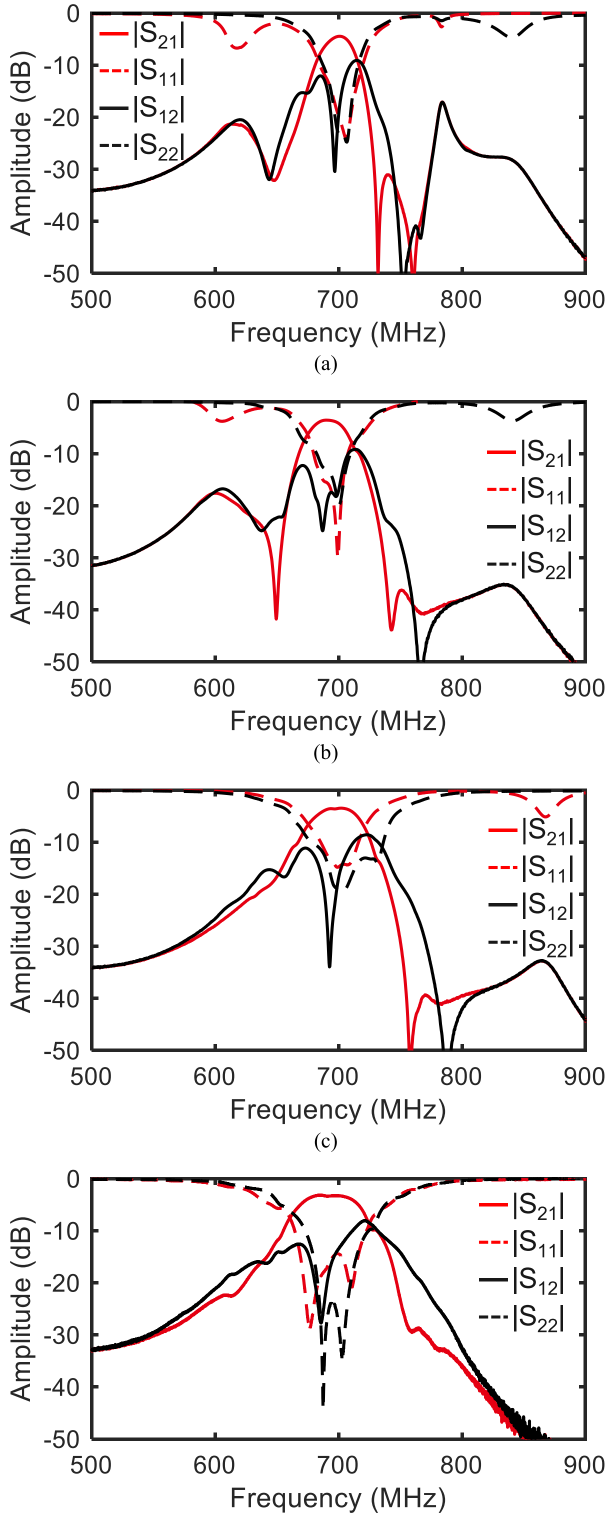

Fig. 25. RF measured TZ reconfiguring capabilities of Filter 4 when operating at its single-band mode. (a) Three TZs. (b) Two TZs. (c) One TZ. (d) No TZ.

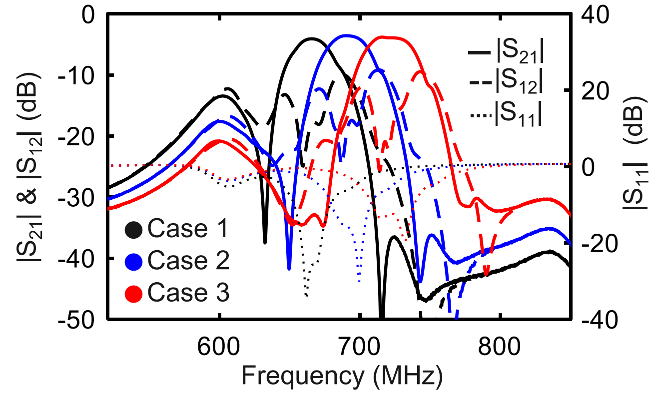

Fig. 26. RF measured f_{cen} tuning capabilities of Filter 4 when operating at its single-band mode.

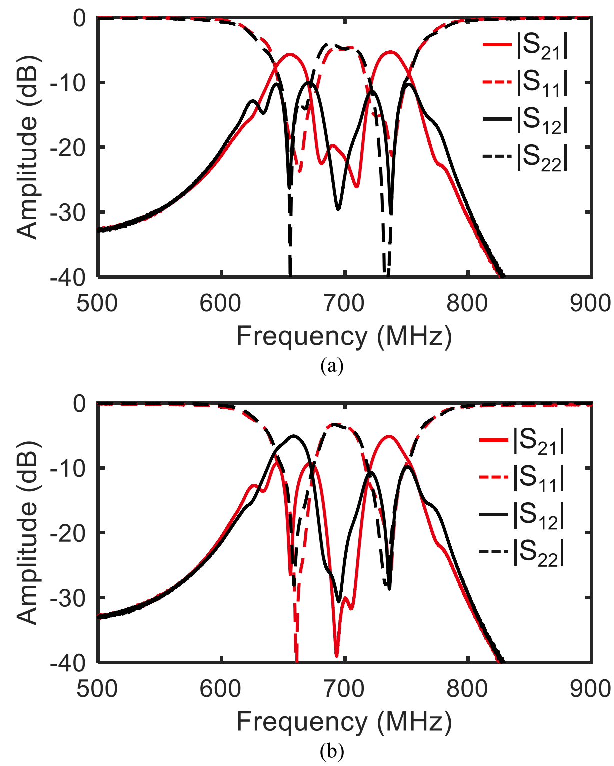

Fig. 27. RF measured reconfigurable capabilities of Filter 4 when operating at its dual-band mode. (a) Both bands transmit in the same direction. (b) Each band is transmitting in a different direction.

tuning states shown in Fig. 25. Fig. 26 shows center frequency tuning when the filter is operating as a single band BPF. Its passband can be tuned from 659-724 MHz with IL between 3.6-4.1 dB and IS $>$ 20 dB.

The dual band state tuning capabilities are demonstrated in Figs. 27 and 28. Specifically, when reconfiguring the sign of the phase progression of the resonators in each band, the direction of propagation can be tuned as shown in Fig. 27(a) and (b) by altering θ from 65° to $-65°$. Furthermore, Fig. 28(a) and (b) show how the two passbands can be tuned independently. Specifically, the lower passband can be tuned between 600-680 MHz with IL between 5.6-6 dB and IS between 23-26 dB. The upper band can be tuned between 716-831 MHz with IL between 4.8-6.2 dB and IS between 25-31 dB. Furthermore, Filter 4 can be intrinsically switched-off as demonstrated in Fig. 29. Return loss for all prototypes is better than 10 dB throughout the entire tuning range.

A comparison of the transversal-cell-based NR-BPF concept with state-of-the-art STM-based non-reciprocal BPFs is

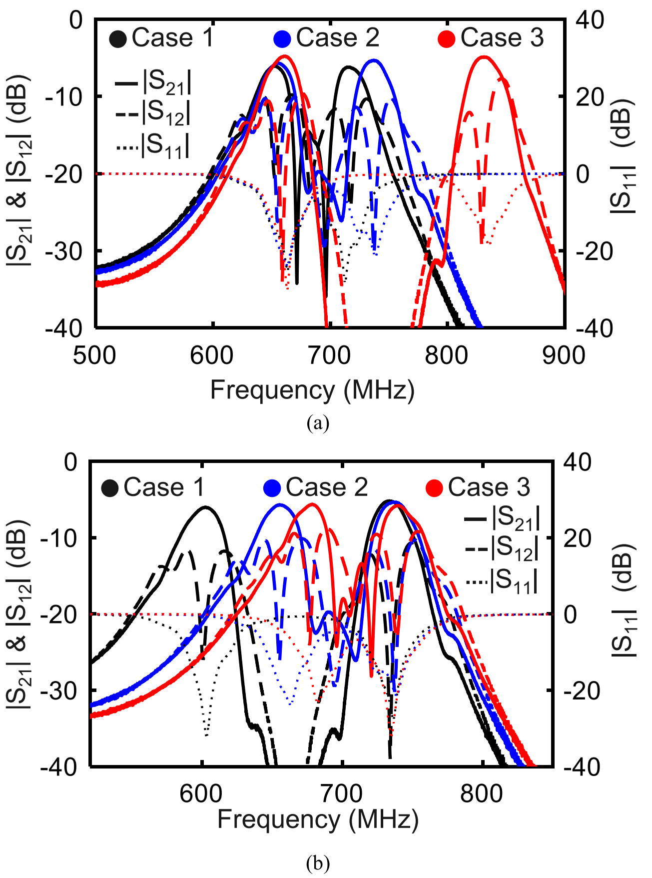

Fig. 28. RF measured f$_{cen}$ tuning capabilities of Filter 4 when operating at its dual-band mode of operation. (a) Upper band f$_{cen}$ tuning. (b) Lower band f$_{cen}$ tuning.

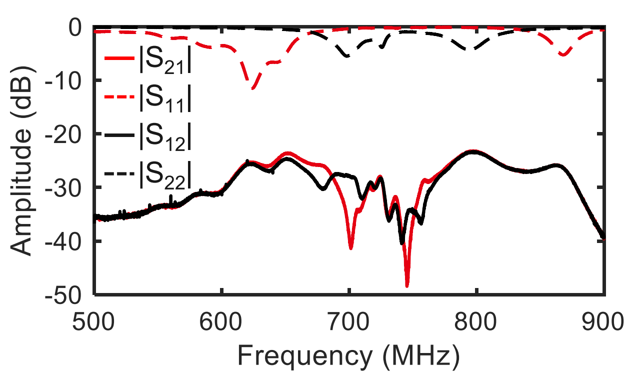

Fig. 29. RF measured intrisnic switching off tuning state of Filter 4.

provided in Table II. As shown, Filters 1, 2, and 3 showcase competitive performance in terms of tuning range, isolation, and return loss when compared to the state-of-the-art. Filters 1 to 3 also exhibit higher order when compared to many existing STM-based non-reciprocal BPFs [13], [16], [17], [18], [20], [21], [22], [23], [24], having higher selectivity and out-of-band rejection. Moreover, Filter 4 shows the highest levels of reconfigurability among all the existing NR-BPFs. It can support both single- and dual-band transfer functions and offers independent tuning of two passbands. Moreover, it can reconfigure its out-of-band response with various TZ configurations, providing improved flexibility in adapting to different system requirements and operating conditions. Furthermore, the proposed filters can be intrinsically switched-off, and can be exploited to reduce the number of RF switches in the RF front-end.

TABLE II

Comparison With the State-of-Art Non-Reciprocal Filters

Ref.	f_{cen} MHz	BW MHz	IL dB	IS dB	IIP3 dBm	OFF
[16]	270~310 (1.14)	15~41.5 (2.8)	1.7~4.3	6.9~30.9	N/A	Yes
[17]	188~202 (1.07) 237~257 (1.08)	14.5, 14	3.7, 5.5 (min)	26.1, 35.9 (max)	N/A	No
[18]	198~224 (1.13) 249~291 (1.17)	13, 21.8	2.9, 2.6 (min)	8.4~44.8, 8~44.3	N/A	No
[19]	900	57	4.4	18	N/A	No
[24]	885~1031 (1.16)	42	3.9~4.6	20~30	11.8	No
Filter 1	570~724 (1.27)	37.5~73.9 (1.87)	4.8~6.8	21~35	-1~13	Yes
Filter 2	630~735 (1.17)	24.8~58 (2.34)	4.8~6.8	20~40	-4~13	Yes
Filter 3	655~760 (1.16)	53~84 (1.57)	4.5~6.7	27~45	0~13	Yes
Filter 4 (Single-band)	665~723 (1.09)	26,34,44,56	3.2~4.5	>25	6.4~10.3	Yes
Filter 4 (Dual-band)	600~680 (1.13), 716~831 (1.16)	25, 29	5.6~6, 4.8~6.2	23~26, 25~31	0~10, 5~13	Yes

V. Conclusion

This paper reported on a comprehensive design methodology for reconfigurable NR-BPFs using STM transversal cells. The proposed method was applied to the design of four filter topologies and demonstrated the potential to achieve single- and multi-band non-reciprocal transfer functions with enhanced reconfigurability. Four proof-of-concept prototypes were manufactured and measured and validated the effectiveness of the transversal cell-based NR-BPF concept in achieving wider tuning ranges, high isolation levels, and superior reconfigurability compared to state-of-the-art STM-based non-reciprocal BPFs. These results underline the potential of using STM transversal cells in designing multi-functional RF components for emerging RF communication systems.

References

[1] A. Nagulu, T. Chen, G. Zussman, and H. Krishnaswamy, "A full-duplex radio using a CMOS non-magnetic circulator achieving +95 dB overall SIC," in *Proc. USNC-URSI Radio Sci. Meeting (Joint AP-S Symp.)*, Jul. 2019, pp. 71–72.

[2] N. Reiskarimian, A. Nagulu, T. Dinc, and H. Krishnaswamy, "Nonreciprocal electronic devices: A hypothesis turned into reality," *IEEE Microw. Mag.*, vol. 20, no. 4, pp. 94–111, Apr. 2019.

[3] X. Li, E. Li, and G. Guo, "Design of X-band H-plane waveguide Y-junction circulator," in *Proc. Int. Workshop Microw. Millim. Wave Circuits Syst. Technol.*, Apr. 2012, pp. 1–4.

[4] H. Dong, J. R. Smith, and J. L. Young, "A wide-band, high isolation UHF lumped-element ferrite circulator," *IEEE Microw. Wireless Compon. Lett.*, vol. 23, no. 6, pp. 294–296, Jun. 2013.

[5] G. Deng et al., "A compact E-plane four-port junction circulator," *IEEE Microw. Wireless Compon. Lett.*, vol. 29, no. 10, pp. 655–658, Oct. 2019.

[6] A. Ashley and D. Psychogiou, "RF co-designed bandpass filter/circulator with tunable center frequency, bandwidth, and out-of-band isolation," *IEEE Microw. Wireless Compon. Lett.*, vol. 31, no. 7, pp. 845–848, Jul. 2021.

[7] D. G. Haigh, "Wideband active microwave isolators using GaAs MMIC technology," *IEE Proc.-Microw., Antennas Propag.*, vol. 143, no. 2, pp. 179–183, Apr. 1996.

[8] S. W. Y. Mung and W. S. Chan, "Active three-way circulator using transistor feedback network," *IEEE Microw. Wireless Compon. Lett.*, vol. 27, no. 5, pp. 476–478, May 2017.

[9] J.-F. Chang, J.-C. Kao, Y.-H. Lin, and H. Wang, "Design and analysis of 24-GHz active isolator and quasi-circulator," *IEEE Trans. Microw. Theory Techn.*, vol. 63, no. 8, pp. 2638–2649, Aug. 2015.

[10] S. A. Ayati, D. Mandal, B. Bakkaloglu, and S. Kiaei, "Integrated quasi-circulator with RF leakage cancellation for full-duplex wireless transceivers," *IEEE Trans. Microw. Theory Techn.*, vol. 66, no. 3, pp. 1421–1430, Mar. 2018.

[11] S. Qin, Q. Xu, and Y. E. Wang, "Nonreciprocal components with distributedly modulated capacitors," *IEEE Trans. Microw. Theory Techn.*, vol. 62, no. 10, pp. 2260–2272, Oct. 2014.

[12] S. Qin and Y. E. Wang, "Parametric conversion with distributedly modulated capacitors (DMC) for low-noise and non-reciprocal RF front-ends," in *IEEE MTT-S Int. Microw. Symp. Dig.*, Jun. 2013, pp. 1–3.

[13] X. Wu, X. Liu, M. D. Hickle, D. Peroulis, J. S. Gómez-Díaz, and A. Álvarez Melcón, "Isolating bandpass filters using time-modulated resonators," *IEEE Trans. Microw. Theory Techn.*, vol. 67, no. 6, pp. 2331–2345, Jun. 2019.

[14] C. Cassella et al., "Radio frequency angular momentum biased quasi-LTI nonreciprocal acoustic filters," *IEEE Trans. Ultrason., Ferroelectr., Freq. Control*, vol. 66, no. 11, pp. 1814–1825, Nov. 2019.

[15] C. Cassella, M. Pirro, G. Michetti, and M. Rinaldi, "Ultra-high isolation nonreciprocal acoustic filters," in *IEEE MTT-S Int. Microw. Symp. Dig.*, Jun. 2019, pp. 524–527.

[16] D. Simpson and D. Psychogiou, "Fully-reconfigurable non-reciprocal bandpass filters," in *IEEE MTT-S Int. Microw. Symp. Dig.*, Aug. 2020, pp. 807–810.

[17] D. Simpson, P. Vryonides, S. Nikolaou, and D. Psychogiou, "Tunable multi-band non-reciprocal bandpass filters," in *IEEE MTT-S Int. Microw. Symp. Dig.*, Jun. 2022, pp. 179–182.

[18] D. Simpson and D. Psychogiou, "Multiband magnetless isolators and circulators with reconfigurable bandpass filtering capabilities," *IEEE Trans. Microw. Theory Techn.*, vol. 71, no. 3, pp. 1239–1250, Mar. 2023.

[19] A. Alvarez-Melcon, X. Wu, J. Zang, X. Liu, and J. S. Gomez-Diaz, "Coupling matrix representation of nonreciprocal filters based on time-modulated resonators," *IEEE Trans. Microw. Theory Techn.*, vol. 67, no. 12, pp. 4751–4763, Dec. 2019.

[20] G. Chaudhary and Y. Jeong, "Nonreciprocal bandpass filter using mixed static and time-modulated resonators," *IEEE Microw. Wireless Compon. Lett.*, vol. 32, no. 4, pp. 297–300, Apr. 2022.

[21] G. Chaudhary and Y. Jeong, "Frequency tunable impedance matching nonreciprocal bandpass filter using time-modulated quarter-wave resonators," *IEEE Trans. Ind. Electron.*, vol. 69, no. 8, pp. 8356–8365, Aug. 2022.

[22] G. Chaudhary, J. Lee, P. Pech, and Y. Jeong, "Microstrip line non-reciprocal bandpass filter with tunable center frequency," in *Proc. IEEE Int. Symp. Radio-Freq. Integr. Technol. (RFIT)*, Jul. 2022, pp. 188–190.

[23] X. Wu, M. Nafe, A. A. Melcón, J. S. Gómez-Díaz, and X. Liu, "A non-reciprocal microstrip bandpass filter based on spatio-temporal modulation," in *IEEE MTT-S Int. Microw. Symp. Dig.*, Jun. 2019, pp. 9–12.

[24] X. Wu, M. Nafe, A. Á. Melcón, J. S. Gómez-Díaz, and X. Liu, "Frequency tunable non-reciprocal bandpass filter using time-modulated microstrip $\lambda_g/2$ resonators," *IEEE Trans. Circuits Syst. II, Exp. Briefs*, vol. 68, no. 2, pp. 667–671, Feb. 2021.

[25] J. Zang, S. Wang, A. Alvarez-Melcon, and J. S. Gómez-Díaz, "Nonreciprocal filtering power dividers," *AEU Int. J. Electron. Commun.*, vol. 132, p. 153690, Apr. 2021.

[26] J. Zang, S. Wang, J. Pan, S. An, and L. Chen, "Magletless nonreciprocal filtering duplexing antenna," *Microw. Opt. Technol. Lett.*, vol. 64, no. 3, pp. 578–582, 2022.

[27] J. Zang, X. Wang, A. Alvarez-Melcon, and J. S. Gomez-Diaz, "Nonreciprocal Yagi–Uda filtering antennas," *IEEE Antennas Wireless Propag. Lett.*, vol. 18, no. 12, pp. 2661–2665, Dec. 2019.

[28] Y. Hadad, J. Soric, and A. Aló, "Spatiotemporally modulated antennas," in *Proc. CNC/USNC URSI Nat. Radio Sci. Meeting*, 2015, p. 159.

[29] S. Taravati and C. Caloz, "Mixer-duplexer-antenna leaky-wave system based on periodic space-time modulation," *IEEE Trans. Antennas Propag.*, vol. 65, no. 2, pp. 442–452, Feb. 2017.

[30] C. Kurth, "Steady-state analysis of sinusoidal time-variant networks applied to equivalent circuits for transmission networks," *IEEE Trans. Circuits Syst.*, vol. CS-24, no. 11, pp. 610–624, Nov. 1977.

[31] D. M. Pozar, *Microwave Engineering*. Hoboken, NJ, USA: Wiley, 2012.

[32] J.-S. Hong and M. J. Lancaster, *Microstrip Filters for RF / Microwave Applications*. Hoboken, NJ, USA: Wiley, 2004.

Zixiao Zhang (Graduate Student Member, IEEE) received the bachelor's and master's degrees from the Huazhong University of Science and Technology in 2016 and 2019, respectively. She is currently pursuing the Ph.D. degree in electrical and electronic engineering with University College Cork (UCC), Ireland. Her current research interests include synthesis, design, and characterization of reconfigurable RF components.

Dimitra Psychogiou (Senior Member, IEEE) received the Dipl.-Eng. degree in electrical and computer engineering from the University of Patras, Patras, Greece, in 2008, and the Ph.D. degree in electrical engineering from the Swiss Federal Institute of Technology (ETH), Zürich, Switzerland, in 2013. She is currently a Professor of electrical and electronic engineering with University College Cork (UCC) and the Head of the Advanced RF Technology Group, Tyndall National Institute, Cork, Ireland. Prior to joining UCC, she was a Sr. Research Scientist with Purdue University, West Lafayette, IN, USA and an Assistant Professor with the University of Colorado Boulder, Boulder, CO, USA. Her research has been presented in more than 230 publications. Her current research interests include RF design and characterization of reconfigurable microwave and millimeter-wave passive components, RF-MEMS, acoustic wave resonator-based filters, tunable filter synthesis, frequency-agile antennas, and additive manufacturing technologies for 3D antenna sub-systems. She is a Senior Member of URSI and a member of the IEEE MTT-S Filters and Passive Components (MTT-5) and Microwave Control Materials and Devices (MTT-13) committees. She has received multiple awards, including the 2023 IEEE MTT-S Outstanding Young Engineer Award, the 2021 Roberto Sorrentino Prize, the SFI Research Professorship Award, the 2020 NSF CAREER Award, the 2020 URSI Young Scientist Award, and the Junior Faculty Outstanding Research Award from UC Boulder. She is the Chair of MMT-13 and the Secretary of the USNC-URSI Commission D. She was an Associate Editor of the *IET Microwaves, Antennas and Propagation*. She is an Associate Editor of the IEEE MICROWAVE AND WIRELESS COMPONENTS LETTERS and the *International Journal of Microwave and Wireless Technologies*. Furthermore, she serves on the technical review board for various IEEE and EuMA conferences and journals.